PCCP

PAPER

View Article Online
View Journal

Cite this: DOI: 10.1039/d6cp01431c

Unlocking the catalytic role of oxygen functionalities on carbon-based catalysts for hydrogen generation from ammonia borane

Elisabetta Inico,[b] Silvio Bellomi,[a] Marta Stucchi,[a] Laura Prati,[a] Alberto Villa,[a] Giovanni Di Liberto *[b] and Ilaria Barlocco *[a]

Received 17th April 2026,
Accepted 30th May 2026

DOI: 10.1039/d6cp01431c

rsc.li/pccp

Carbon-based materials are steadily emerging as a potential solution to reduce the use of metals in hydrogen generation. The role of the amount of different oxygen-based functional groups in the ammonia borane hydrolytic decomposition to hydrogen was investigated by functionalising with a strong oxidising agent, HNO_3, carbon materials with different graphitisation degrees, *i.e.*, pyrolitically stripped carbon nanofibers (CNFs), graphite and graphene nanoplates (GNP). Results obtained with XPS and Raman spectroscopy studies indicate that the oxygen content increases due to an increase in the quantity of defects in the original materials: O-GNP < O-Graphite ≪ O-CNFs. In order to further refine the results in terms of the nature of the oxygen functionalities introduced, a mild oxidising agent was also employed on CNFs, *i.e.* hydrogen peroxide (H_2O_2). Indeed, carbonyl and carboxyl groups are predominant under strong oxidizing conditions, while ether-like and hydroxyl groups were introduced using H_2O_2. The presence of C═O bonds has a positive effect on hydrogen production, resulting in an increase of approximately one order of magnitude from O-Graphene to O-CNFs. Quantum chemical density functional theory calculations were used to obtain some atomistic insight into the activation of ammonia borane and to assess the effect of oxygen functionality. The results of this study provide evidence of the positive effects induced by the presence of C–O double bonds, suggesting a viable method for further catalytic optimization toward the generation of hydrogen from ammonia borane.

Introduction

Hydrogen is a potential carbon-neutral energy source, but developing effective and safe hydrogen storage technologies remains a huge challenge.[1,2] Liquid hydrogen carriers have been demonstrated to be excellent for large-scale and long-distance hydrogen transportation and storage because of their safety, efficiency, environmental friendliness and above all high hydrogen storage capacity.[3–5] Noble metal-based catalysts are typically employed to quickly decompose these compounds into ultra-pure hydrogen at moderate temperatures.[6–12] This raises some questions on the overall sustainability of the process, triggering attention towards metal-free alternatives.[13–15] Carbon-based materials are a promising solution to reduce the use of metals in heterogeneous catalysis. For instance, carbocatalysts have been widely investigated in gas phase reactions, *e.g.* dehydrogenation of alkanes and alkenes.[16–18] These materials were also efficiently applied in photocatalytic and electrocatalytic processes.[19,20] Importantly, carbon-based materials were also employed in liquid phase reactions,[21] such as reductions of C–C multiple bonds and aromatic compounds,[22,23] coupling reactions[24,25] and alcohol oxidation.[26,27] The surface structure of a carbocatalyst can be controlled by the experimental conditions, making them a workhorse in heterogeneous catalysis. Indeed, the combination of topological defects (*i.e.* vacancies and reconstructions) and heteroatoms (such as O, N, B and P)[28–31] leads to a large number of possible changes of the surface, which reflects the catalytic activity.[32–40]

Carbocatalysts have recently been used in hydrogen production from liquid hydrogen carriers. Some of us[41,42] showed that intrinsic carbon defects, and in particular single vacancies, are active in formic acid and hydrazine dehydrogenation, by combining experiments and quantum chemical calculations. Moreover, we demonstrated that oxygen functionalities are active in hydrazine decomposition.[43] In particular, carboxyl and carbonyl groups are responsible for decomposing the molecule towards hydrogen and nitrogen.

A promising storage medium for hydrogen is ammonia borane. Ammonia borane is a model liquid hydrogen carrier

[a] Department of Chemistry, Università degli Studi di Milano, Via Golgi 19, 20133, Milano, Italy. E-mail: ilaria.barlocco@unimi.it
[b] Department of Materials Science, University of Milano-Bicocca, Via Cozzi 55, 20125, Milano, Italy. E-mail: giovanni.diliberto@unimib.it

because it has high density, nontoxicity, and moderate decomposition temperature. In addition, it is stable in air and soluble in water and other polar solvents.[44] Moreover, NH_3BH_3 has a high hydrogen storage capacity of 19.6 wt% and it is composed of only non-toxic elements. Ammonia borane can be decomposed to give hydrogen either *via* pyrolysis (in solid state) or by metal-catalysed reaction in the presence of water (*via* hydrolysis).[45,46] During thermolysis, ammonia borane can rapidly provide high-quality H_2, but its application is still hindered by two issues: (1) the dehydrogenation temperature needs to be reduced (at least under 85 °C, the fuel cell operating temperature), and (2) the formation of volatile by-products needs to be inhibited.[24] In contrast, hydrolytic dehydrogenation can be achieved under mild reaction conditions (room temperature and pressure). The catalysts employed in this reaction are usually noble-metal based (*e.g.* Pt, Rh, Pd and Ru)[47–51] supported on oxides, such as CeO_2.[46] In this reaction, water is not only the solvent, but also a hydrogen source, see eqn (1). According to this path, 3 moles of hydrogen can be released per mole of ammonia borane provided that a metal catalyst is present.[52] This reaction involves the cleavage of B–H and O–H bonds, in ammonia borane and H_2O molecules, respectively. Moreover, a catalyst needs to facilitate H* transfer to evolve H_2.[53]

Hydrolytic dehydrogenation:

$$NH_3BH_3(aq) + 2H_2O(l) \rightarrow NH_4BO_2(aq) + 3H_2(g) \quad (1)$$

Given the potential of oxygen-functionalized carbocatalysts for hydrogen generation from hydrazine, in this work, we investigated the effect of the amount and nature of oxygen functional groups on carbon materials with different graphitisation degrees on the liquid phase hydrolytic decomposition of ammonia borane (AB) to form hydrogen under mild reaction conditions. Experimental data were combined with density functional theory calculations to provide insights into the role of oxygen functionalities and to provide an understanding of the activation of ammonia borane on carbocatalysts. The amount of the introduced groups was modulated by employing materials with different degrees of graphitization, as it has been shown that the most reactive carbon sites are associated with vacancies, which serve as the primary sites for functionalization.[54]

Moreover, to further refine the results in terms of the nature of the groups, two oxidising agents were selected (*i.e.* H_2O_2 and HNO_3). Based on the combination of experimental data and DFT calculations, the increase in the number of C–O double bonds has a positive effect, with an increase in the reaction yield by about one order of magnitude. The results of this study provide insights into the activation of ammonia borane and indicate a potential way for further optimization of the catalyst. Indeed, this study aims to demonstrate the possibility of decomposing this substrate into hydrogen without the use of a metal, without claiming to be the most effective catalyst. Nevertheless, to the best of our knowledge, this is the first example of a metal-free catalyst for AB hydrolytic dehydrogenation.

Experimental section

Materials and chemicals

Ammonia borane (NH_3BH_3, 90%), nitric acid (HNO_3, 65%) and hydrogen peroxide (H_2O_2, 30%) were purchased from Sigma-Aldrich, while pyrolytically stripped carbon nanofibers, CNFs, from Applied Science Company. Graphite was purchased from Johnson Matthey and graphene nanoplates (GNP) from XG Sciences Inc. (Lansing, MI, USA).

Catalyst synthesis

Carbon materials were functionalised by employing a previously reported method.[43] In this procedure, 1 g of selected carbon was dispersed in 200 mL of the selected oxidising agent (HNO_3 65% or H_2O_2 30% in water) in a 500 mL round bottom flask.

HNO_3 oxidation: the dispersion was stirred at 800 rpm for 6 hours at a temperature of 353 K, then the obtained catalyst was filtered and washed with milliQ water until a neutral pH was obtained. The solid was then dried in an oven at 353 K for 4 hours. Herein, O-CNFs-HNO_3, O-graphite and O-GNP were obtained.

H_2O_2 oxidation: the dispersion was stirred at 800 rpm for 1 hour at room temperature. Also in this case, the material was filtered and washed with milliQ water until a neutral pH was obtained. The solid was then dried in an oven at 353 K for 4 hours. Herein, O-CNFs-H_2O_2 was obtained.

Catalytic tests

The hydrolytic dehydrogenation of ammonia borane was performed at a constant reaction temperature of 323 K, in a 27 mL two-necked round bottom flask. The reaction conditions were selected after optimisation. A temperature of 323 K produced the best ratio between catalytic activity and environmentally friendly conditions. H_2 evolution was monitored through the Man on the Moon X104 kit, measuring the partial pressures of the released product.[55–57] The setup was equipped with an HCl trap that can capture NH_3. With this system, the pressure observed is only due to the presence of H_2, so the conversion of AB observed is equal to the yield of H_2 produced. The selected amount of catalyst (15 mg) was inserted in the reactor with 5 mL of deionised water and heated at the selected temperature. When the system reached equilibrium, 400 μL of a 1 M AB solution was injected and stirred at 1400 rpm, starting the reaction. The kinetic profiles were collected until the reaction was completed, indicated by the pressure plateau, collecting 0.5 points per s. In order to confirm experimental reproducibility, catalytic tests were repeated at least three times.

Characterisation

Raman spectroscopy was performed by employing a Horiba LabRam HR Evolution micro-Raman spectrometer equipped with a green solid-state laser (532 nm) focused through a 100× objective, giving a spatial resolution of approximately 1 μm. The system was set with a 300 μm size hole and a 600 lines per mm grating. The final laser power was about 0.05 mW. The calibration was performed by employing a silicon wafer and using a 520.7 cm^{-1} line. A hand-held power meter was used to measure

the sample surface. The samples were scanned for 300 s, performing two accumulations.

X-Ray photoelectron spectroscopy (XPS) measurements were carried out with a Thermo Scientific K-alpha+ spectrometer. The spectra were collected by using a monochromatic Al X-ray source operating at 72 W, with the signal averaged over an oval-shaped area of 600 × 400 μm. Data were recorded at 150 eV for survey scans and 40 eV for high-resolution (HR) scans with a 1 eV and 0.1 eV step size, respectively. CASAXPS (v2.3.17 PR1.1) was used to analyse the XPS raw data.

Inductively coupled plasma optical emission spectroscopy (ICP-OES) was performed by a PerkinElmer Optima 8000 emission spectrometer.

Computational details

Spin polarized density functional theory (DFT) calculations were performed with the VASP code[58–60] using the generalized gradient approximation, as implemented in the Perdew–Burke–Ernzerhof (PBE) functional.[61] Single point PBE0[62,63] calculations have been performed to refine the electronic structure.[64] This is typically a reasonable choice to provide accurate results without the need to perform computationally demanding geometry optimizations with hybrid functionals. The valence electrons were expanded on a set of plane waves with a kinetic energy cutoff of 400 eV, and the core electrons were treated with the projector augmented wave (PAW) approach.[65,66] The threshold criteria for electronic and ionic optimizations were set to 10^{-5} eV and 10^{-2} eV Å^{-1}, respectively. The sampling of the reciprocal space was adapted to provide converged results.

Previous studies by some of us on graphene nanosheets for catalysis have deeply assessed the accuracy of computational protocols, including the sampling of the k-point. In particular, it has been demonstrated that for the working simulation cell, a 4 × 4 × 1 grid allows for reasonably converged results with respect to 5 × 5 × 1 or denser grids.[67] Dispersion forces have been included according to Grimme's D3 parametrization.[68]

We simulated a graphene nanosheet obtained upon full optimization of the unit cell and generation of a supercell. The working lattice vectors are a = 9.870 Å, b = 9.870 Å, and γ = 120°,[69,70] considering the presence of a vacuum layer of 15 Å to avoid spurious effects due to interaction between periodic replicas of the system along the nonperiodic direction. The functionalities were created following previous works by some of us.[43] We created a carbon vacancy and functionalized a carbon atom with hydroxyl (C–OH), carbonyl (C═O), and carboxyl (COOH) groups. Also, the ether defect (C–O–C) was modelled by putting the O atom in the empty carbon lattice site. In each case, the atomic coordinates were fully relaxed.

The Gibbs energies were evaluated by adopting the *ab initio* thermodynamic approach,[71,72] by adding to the DFT energy the contribution of zero-point energy correction and entropy terms (Table S4). The first were calculated in a harmonic fashion. The entropies of gas-phase species were taken from the international tables, and the entropy of solid-state species was determined through the formalism of the partition function.[73] The Gibbs free energy profiles were determined under the following reaction conditions: T = 323 K and P = 1 atm.

Results and discussion

The role of different graphitisation degrees on the introduction of oxygen functionalities was investigated in the ammonia borane hydrolytic decomposition to hydrogen by employing materials with different defect densities, *i.e.* pyrolitically stripped carbon nanofibers (CNFs), graphite and graphene nanoplates (GNP). The use of carbonaceous materials with different defectivity enables us to study the amount of the introduced oxygen functional groups, as it has been shown that the most reactive carbon sites are associated with vacancies, which serve as the primary sites for functionalization.[54] The selected bare carbons were firstly modified by using HNO_3, a strong oxidising agent.

The physical properties of these materials pre- and post-treatment are reported in Table S1. The oxidative treatments increased surface functionalization in the presence of a high number of defects, but did not significantly affect either the structure and size or the grain shape.[74] ICP-OES, Raman spectroscopy and XPS were employed to understand the composition and fine structure of the different catalysts. ICP-OES confirmed the metal-free nature of the materials selected, confirming the absence of metal impurities.[41,42] Then, we evaluated possible modifications in the catalyst morphology by Raman spectroscopy.[75–78] Indeed, the defects in carbons can be quantified by evaluating the intensity of their two characteristic bands, one at around 1600 cm^{-1} (G band) and the other at 1350 cm^{-1} (D band).[78] Their ratio (I_D/I_G) describes the defect density since the G band indicates the structurally ordered graphitic domains, while the D band is symmetry forbidden and only allowed when defects and substitutional heteroatoms are present in the structure.[77,79,80] So, when the ratio between the two bands increases, it is indicative of a defective material, while a low I_D/I_G value indicates a graphitic carbon with a small number of defects. Table S1 reports the values of I_D/I_G ratios, showing that no substantial modification in the intrinsic defects and in the addition of substitutional heteroatoms is present after the functionalisation procedure, see also Fig. S1. The survey XPS spectra were employed to quantify the relative carbon and oxygen ratio (O/C, see Table S1 in the SI), showing an increase in the oxygen content by increasing the number of defects in the material. Indeed, CNFs have the most defective material (I_D/I_G = 0.86 and O/C = 0.122) and after the functionalisation process, the O-content increased to 0.181 for O-CNFs-HNO_3. Considering graphite (I_D/I_G = 0.09 and O/C = 0.02), the amount of oxygen only slightly increased to 0.07 for O-graphite, while the O/C ratio of pristine and modified GNP remained the same (O/C = 0.03).

From the high-resolution (HR) O1s and C1s spectra, we can gain information about the type and quantity of the oxygen functional groups introduced (Fig. S2 and Tables S2, S3).[43,80] In particular, five peak regions, as identified in previous studies,

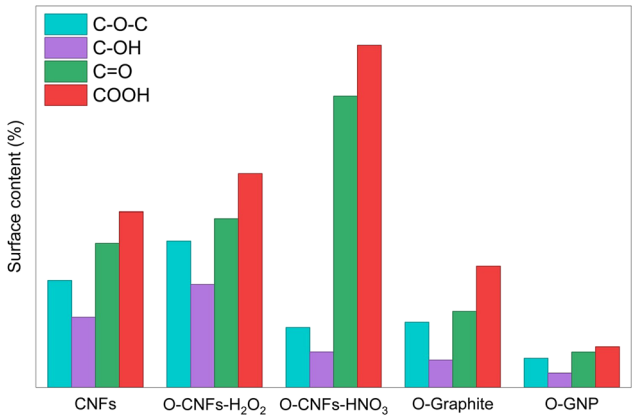

Fig. 1 Type and quantity of oxygen-based functional groups for different carbocatalysts obtained from the analysis of the HR-XPS O1s spectrum and normalised for the O/C content.

were found in the O1s core levels.[81] Starting from low binding energies (BE), the peak between 531.1 and 531.8 eV can be assigned to carbon–oxygen double bonds (C═O), followed by those in the 532.0–533.0 eV region due to carboxylic groups (COOH). The carbon–oxygen single bonds, like ether, can be found in the BE region 532.4–532.7 eV. Hydroxyl groups came next within 533.3 and 533.6 eV. A broad peak near 535.2 eV can be ascribed to residual adsorbed water on the catalyst's surface. Fig. 1 shows the nature and quantity of the different O-functional groups present on the surface of the catalysts. Their amount was obtained from the HR-XPS O1s spectrum (Table S3) and normalised for the O/C content (Table S1). After treating CNFs with HNO_3, carbonyl and carboxyl groups increased from 3.21% (C═O) and 3.91% (COOH) before oxidation to 6.49% (C═O) and 7.62% (COOH), as expected. On the other hand, ether-like and hydroxyl groups notably diminished from 1.56% to 0.79% (C–OH) and from 2.38% to 1.33% (C–O–C), respectively. These results are consistent with previous works.[43] Because of the scarcity of defectivity on graphite and GNP, the oxygen content remains low also after the treatment with a strong oxidising agent. For graphite, the amounts of ether-like and hydroxyl groups are found to be 1.45% and 0.61%, respectively. The majority of the groups inserted contain CO double bonds, *i.e.* C═O = 1.69% and COOH = 2.70%. A similar scenario was observed on GNP, where C–O–C and C–OH groups represent 0.65% and 0.32%, while C═O and COOH represent 0.79% and 0.90%, respectively.

In order to further refine the results in terms of the nature of the oxygen functionalities introduced, a mild oxidising agent was also employed on CNFs, *i.e.* hydrogen peroxide (H_2O_2). Due to the negligible oxygen incorporation observed in GNP and graphite compared to CNFs, the treatment with H_2O_2 was restricted to CNFs, in order to ensure statistically meaningful and detectable differences. Indeed, it is well known that the use of a strong oxidising agent, such as nitric acid (HNO_3), can preferentially introduce groups containing carbon–oxygen double bonds, *i.e.* carbonyl and carboxyl (C═O and HO–C═O).[82–86] On the other hand, a compound with a milder oxidation strength, such as H_2O_2, can promote the formation of C–O bonds, and in particular hydroxy and ether groups.[87]

Hydrogen peroxide treatment increased the O/C ratio to 0.141, corresponding to an intermediate degree of surface oxidation between bare CNFs and HNO_3-treated CNFs: CNFs (O/C = 0.122) < O-CNFs-H_2O_2 (O/C = 0.141) < O-CNFs-HNO_3 (O/C = 0.181). This progressive increase reflects the oxidizing strength of the treatment, with stronger oxidants promoting more extensive surface oxidation through the generation of defect sites and the incorporation of oxygen-containing functional groups. Fig. 2 shows the HR O1s spectra of the materials with the highest oxygen content. As expected, after H_2O_2 treatment, ether-like and hydroxyl groups increased from 2.38% (C–O–C) and 1.56% (C–OH) before oxidation to 3.26% (C–O–C) and 2.29% (C–OH). The same trend was observed for carbonyl (CNFs: 3.21% and O-CNFs-H_2O_2 : 3.76%) and carboxyl (CNFs: 3.91% and O-CNFs-H_2O_2 : 4.76%) groups, as previously reported.[43]Once the relative amount of oxygen functionalities on carbocatalysts was investigated, we performed the ammonia borane decomposition reaction in a batch reactor under mild reaction conditions (323 K and 1 atm). H_2 evolution was monitored through the Man on the Moon X104 kit, measuring the partial pressures of the released product. The kinetic profiles were collected until the reaction was completed, indicated by a pressure plateau. Fig. 3 reports the time evolution of AB hydrolytic decomposition. O-CNFs-HNO_3 provides the highest H_2

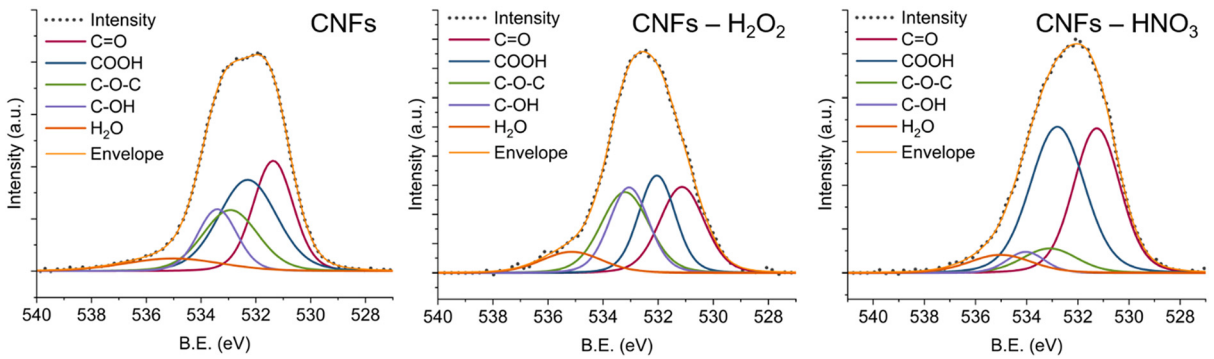

Fig. 2 High resolution analysis of the O1s region of bare and oxidised carbon nanofibers.

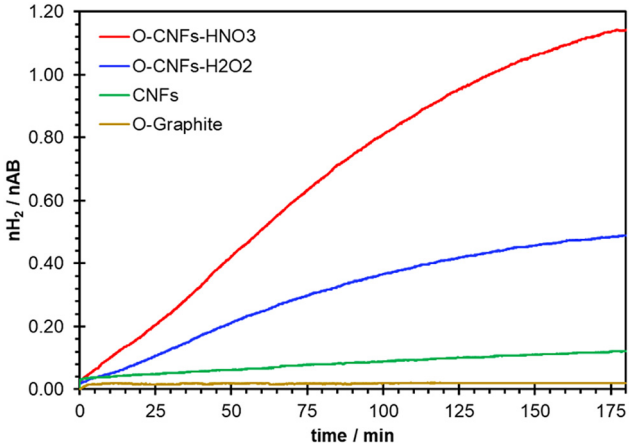

Fig. 3 Kinetic profiles of the active carbocatalysts for ammonia borane decomposition. All tests were performed at least three times at 323 K and 1400 rpm using a 7.4×10^{-2} M AB solution. The error bars were calculated as ±2.5% of nH_2.

production at the end of the reaction (after 180 min of reaction), 4.57×10^{-1} mmol. The H_2 produced by O-CNFs-H_2O_2 is about halved, 2.02×10^{-1} mmol. Bare CNFs showed a very low activity in ammonia borane decomposition, about one order of magnitude lower than O-CNFs-HNO_3, 5.7×10^{-2} mmol. The activity of functionalised graphite (O-Graphite) was almost negligible: 0.9×10^{-2} mmol, while bare graphite, GNP and O-GNP were considered inactive. Indeed, the oxygen content reported in Table S1 is correlated with enhanced H_2 production: O/C content increased in the order graphite (O/C = 0.02, nH_2 at 180′ = 0 mmol) = GNP (O/C = 0.03, nH_2 at 180′ = 0 mmol) = O-GNP (O/C = 0.03, nH_2 at 180′ = 0 mmol) < O-Graphite (O/C = 0.07, nH_2 at 180′ = 0.9×10^{-2} mmol) < CNFs (O/C = 0.122, nH_2 at 180′ = 5.7×10^{-2} mmol) < O-CNFs-H_2O_2 (O/C = 0.141, nH_2 at 180′ = 2.02×10^{-1} mmol) < O-CNFs-HNO_3 (O/C = 0.181, nH_2 at 180′ = 4.57×10^{-1} mmol) indicating the prominent role of the oxygen quantity on the catalyst properties. It is worth noting that, even for the most active catalyst (O-CNFs-HNO_3), the incomplete H_2 release observed may be attributed to the progressive accumulation of borate/polyborate species formed during AB hydrolysis. These by-products can adsorb onto the catalyst surface, partially blocking the active sites and slowing down the reaction kinetics, thereby preventing complete AB conversion within the investigated reaction time.[88–90] Moreover, the nature of the O-functional group seems to be critical.

The increased activity in the presence of carbonyl and carboxyl oxygen functionalities was previously observed by some of us[43] in the hydrazine hydrate dehydrogenation reaction. In this work, the same groups are the most active in decomposing the ammonia borane substrate. These results let us assume that, also in this case, these groups can play a key role in the ammonia borane dehydrogenation reaction. Observing the speciation of the functionalities of the best performing material, O-CNFs-HNO_3, and comparing them with other catalysts, groups containing a C–O double bond are crucial in decomposing ammonia borane to hydrogen.

Indeed, the higher the contribution of C═O and COOH groups, the higher the H_2 production. In the case of O-CNFs-HNO_3 (C═O = 6.49% and COOH = 7.62%), the moles of H_2 produced are 8 times higher than bare CNFs (C═O = 3.21% and COOH = 3.91%). O-CNFs-H_2O_2 shows an intermediate behaviour in terms of activity and C═O/COOH content, 3.76% and 4.76%, respectively. The activity of the remaining carbocatalysts is negligible, in line with their oxygen content. Table 1 summarizes the relationship between H_2 production and the nature and quantity of oxygen functional groups.

Quantum chemical calculations were employed to gain insight into the role of different oxygen functionalities (*i.e.* –OH, C–O–C, C═O and HO–C═O) in activating the B–N bond in ammonia borane. We modelled activation of AB on different model catalysts reported in Fig. 4, which contain the oxygen functionalities reported above. The calculated Gibbs free energy of the total decomposition of ammonia borane to hydrogen is negative, −0.69 eV, indicating that the reaction is exergonic at atmospheric pressure and T = 323 K. The modelling of the full reaction pathway for the decomposition of ammonia borane is extremely complex due to the very large number of possible reaction intermediates that can form.[91] For this reason, we restrict this analysis to the activation of ammonia borane on the model catalysts (Fig. 4). It should be emphasised that, although water is intrinsically involved in the hydrolytic decomposition of ammonia borane and may participate in proton-transfer and hydrogen-evolution steps, the aim of the present study was to elucidate the role of the different oxygen-containing surface functionalities in the activation of the ammonia borane molecule. Accordingly, the computational analysis was restricted to the elementary steps associated with B–N bond cleavage on the model catalytic surfaces, which is expected to represent a key step in the overall hydrolytic decomposition pathway. The calculated Gibbs free energies for ammonia borane activation of different models are reported in Table S4.

Additional calculations, including implicit solvation effects, were performed to estimate the role of the aqueous environment. Although the solvent affects the stability of some

Table 1 H_2 yield and nature and quantity of oxygen functional groups for the different carbocatalysts

Sample name	nH_2 at 180′/mmol × 10^{-2}	C–O–C/%	C–OH/%	COOH/%	C═O/%
CNFs	5.69	2.38	1.56	3.91	3.21
O-CNFs-H_2O_2	20.2	3.26	2.29	4.76	3.76
O-CNs-HNO_3	45.7	1.33	0.79	7.62	6.a49
O-Graphite	0.86	1.45	0.61	2.70	1.69
O-GNP	—	0.65	0.32	0.90	0.79

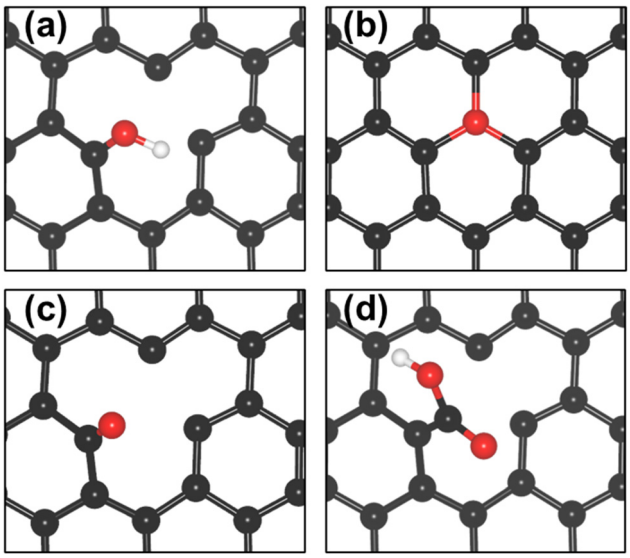

Fig. 4 Different oxygen functionalities investigated in this work: hydroxyl (a), ether (b), carbonyl (c) and carboxyl (d) functional groups.

intermediates, the overall mechanistic picture and the relative reactivity of the different oxygen functionalities remain essentially unchanged (Fig. S4 and Table S5). A more complete description of water effects would require explicit solvent molecules and dynamical simulations,[92] which are beyond the scope of the present study.

Previous works suggested that ammonia borane can be activated in several possible different ways:[46,93] in this work, we explored three possible pathways, all involving the cleavage of the B–N bond. In the first case, NH_3BH_3 is adsorbed on the catalyst according to the following reaction:

$$\text{Pathway a: } NH_3BH_3 + * \rightarrow NH_3* + BH_3* \quad (2)$$

The cleavage of the B–N bond leads to two adsorbates on the catalytic surface, NH_3*, BH_3*. Alternatively, in some cases we found a solution where one B–H bond is broken, forming BH_2* BH_2* and an adsorbed hydrogen atom H*.

$$\text{Pathway b: } NH_3BH_3 + * \rightarrow NH_3* + BH_2* + H* \quad (3)$$

A third possible picture consists of breaking the B–N bond, releasing the ammonium ion in solution, and leaving a boron hydride adduct adsorbed on the surface, $[BH_2]^-*$:

$$\text{Pathway c: } NH_3BH_3 + * \rightarrow NH_4^+{}_{(aq)} + [BH_2]^-* \quad (4)$$

For each surface functionality, all plausible activation pathways were initially explored; however, only the distinct and computationally stable pathways are discussed below, since several initial configurations converged to identical minima during geometry optimisation. We start from the hydroxyl (–OH, Fig. 4a) and ether (C–O–C, Fig. 4b) functionalities, which are those dominant in the carbocatalyst obtained *via* H_2O_2 treatment. In the case of hydroxyl groups, ammonia borane activation *via* B–N bond breaking can occur with the release of ammonium ion in solution (eqn (4)), or with the formation of NH_3* and BH_3* absorbed on the surface (eqn (2)). As it can be seen in Fig. S3, the most stable pathway for the activation involves the breaking of ammonia borane bonds releasing ammonium ions in solution, with a Gibbs free energy of the process equal to −0.20 eV, which is substantially lower than the same value (0.99 eV) for a process involving the formation of both NH_3* and BH_3* on the surface. The picture shown in eqn (3) is not possible for this catalyst. Therefore, the results suggest that the hydroxyl functionality preferentially activates ammonia borane and forms $NH_4^+{}_{(aq)} + [BH_2]^-*$.

Moving to the ether group, the only possible pathway is that reported in eqn (4), where ammonium is released in solution, leaving the boron hydride adduct on the surface. The Gibbs free energy is nearly unchanged with respect to the previous model, −0.22 eV, Fig. S3. This result indicates that hydroxyl and ether groups are expected to have a comparable reactivity.

The carbonyl (C═O, Fig. 4c) and carboxyl (COOH, Fig. 4d) functional groups are the most interesting ones. Indeed, all

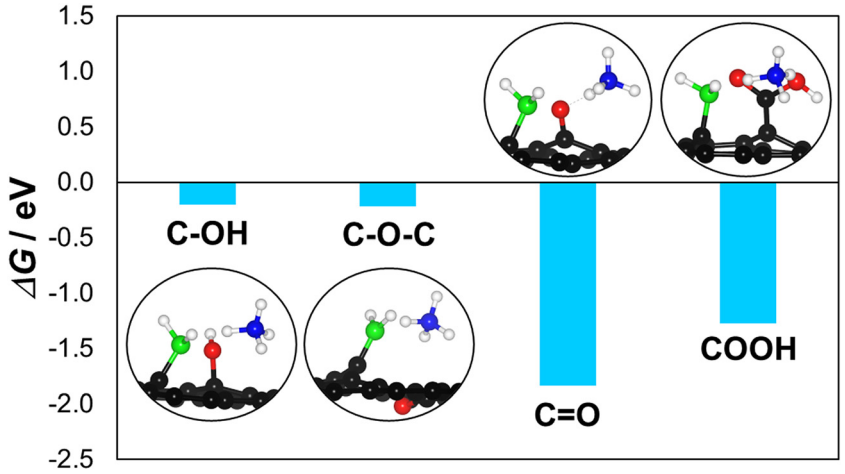

Fig. 5 Gibbs free energy of ammonia borane activation for each functional group. For each system the most stable adsorption pathway is reported; it always corresponds to the pathway reported in eqn (4).

three pathways are possible, Fig. S3, but the most favourable one always proceeds *via* the release of NH_4^+ and formation of the boron hydride adduct on the surface (eqn (4)). Interestingly, the Gibbs free energies of the process are −1.84 eV for carbonyl and −1.27 eV for the carboxyl groups, substantially more negative than those of hydroxyl (−0.20 eV) and ether groups (−0.22 eV). Based on these results, quantum chemical calculations suggest that C–O double bonds are more prone to activate the ammonia borane decomposition reaction than single C–O ones, as reported in Fig. 5, in line with the experimental observation. Indeed, for the carbonyl and carboxyl functionalities, a significant elongation of the C–O bond is observed upon interaction with ammonia borane, amounting to 0.13 Å for C═O and 0.09 Å for COOH. This behaviour is consistent with the stronger interaction of the carbonyl-containing functionalities with respect to hydroxyl groups. In contrast, the C–OH functionality, which interacts only weakly with NH_3BH_3, does not exhibit any significant variation in the bond length (0.01 Å). The situation is more complex for the C–O–C functionality, since structural reconstruction occurs upon interaction with ammonia borane, leading to cleavage of one C–O bond and formation of a dangling bond that can interact with the BH_2 moiety. The values of the C–O bond lengths before and after ammonia borane adsorption are reported in Table S6. Furthermore, in all cases, the preferred thermodynamic path releases ammonium ions in solution, leaving the boron hydride adduct on the surface (eqn (4)). This indicates that hydrogen will evolve from the addition of water to the boron hydride adsorbate. Further work will be dedicated in the near future to further elucidate the way hydrogen is released upon the addition of water to the boron hydride adsorbate.

Conclusions

In this work, we performed a joint experimental and computational study to investigate the role of different oxygen functionalities of carbocatalysts in hydrolytic ammonia borane decomposition to hydrogen. Carbonaceous materials with different defect densities were treated with a strong oxidising agent (HNO_3) to investigate the effect of the amount of oxygen introduced, *i.e.* CNFs, graphite and GNP. Raman and XPS spectroscopy were employed to characterize the nature and quantity of the different functional groups. The scarcity of defectivity of GNP and graphite results in a negligible final oxygen content. In fact, the most reactive carbon sites are associated with vacancies, which serve as the primary sites for functionalization. A different scenario presents for CNFs, where the O/C increased from 0.122 for bare CNFs to 0.181 for O-CNFs-HNO_3. In order to further refine the results in terms of the nature of the oxygen functionalities introduced, a mild oxidising agent was also employed on CNFs, *i.e.* hydrogen peroxide (H_2O_2). When a mild oxidising agent, such as hydrogen peroxide is employed, the content of single C–O species, such as hydroxyl and ether groups, is increased from 1.56% and 2.38%, respectively, for the bare CNFs to 2.29% and 3.26%, respectively, for O-CNFs-H_2O_2. In contrast, the use of a stronger oxidising agent, *i.e.* nitric acid, increases carbon–oxygen double bond content (C═O and COOH). This resulted in an increase in the H_2 production when carbonyl and carboxyl are present, reaching 4.57×10^{-1} mmol, about 8 times higher than the bare CNFs. Quantum chemical density functional theory calculations were used to obtain some atomistic insight into the activation of ammonia borane and to assess the effect of oxygen functionalities on B–N bond activation. Calculations suggest that C–O double bonds are more prone to activate the ammonia borane hydrolytic dehydrogenation than single C–O ones, in line with the experimental observation. In all cases, the preferred activation path releases ammonium ions in solution, leaving a boron hydride adduct on the surface. The release of hydrogen is expected to take place from the addition of water to the adduct. Further investigations will therefore focus on elucidating the explicit role of water in the reaction mechanism and on achieving a more comprehensive understanding of the elementary steps governing ammonia borane hydrolytic decomposition, with the aim of further optimising catalyst performance.

Author contributions

This manuscript was written through contributions from all authors. All authors have given approval to the final version of the manuscript. Elisabetta Inico: formal analysis, data curation and investigation; Silvio Bellomi: data curation and methodology; Marta Stucchi: writing – review & editing and visualization; Laura Prati: writing – review & editing; Alberto Villa: methodology, conceptualization, funding acquisition, project administration and supervision; Giovanni Di Liberto: funding acquisition, investigation, methodology, supervision, writing – original draft, and writing – review & editing; Ilaria Barlocco: conceptualization, data curation, formal analysis, funding acquisition, supervision, writing – original draft, and writing – review & editing.

Conflicts of interest

There are no conflicts to declare.

Data availability

Data will be available on request.

Supplementary information (SI): the following files are available free of charge. Additional characterization and DFT details, *i.e.* Raman and HR-XPS results and Gibbs free energy values and diagrams for each functional group considered (PDF). See DOI: https://doi.org/10.1039/d6cp01431c.

References

1 K. T. Møller, T. R. Jensen, E. Akiba and H. W. Li, Hydrogen—A sustainable energy carrier, *Prog. Nat. Sci.: Mater. Int.*, 2017, **27**, 34–40.

2 T. N. Veziroğlu and S. Şahin, 21st Century's energy: Hydrogen energy system, *Energy Convers. Manage.*, 2008, **49**, 1820–1831.
3 M. Yadav and Q. Xu, Liquid-phase chemical hydrogen storage materials, *Energy Environ. Sci.*, 2012, **5**, 9698–9725.
4 C. Lang, Y. Jia and X. Yao, Recent advances in liquid-phase chemical hydrogen storage, *Energy Storage Mater.*, 2020, **26**, 290–312.
5 H.-L. Jiang, S. K. Singh, J.-M. Yan, X.-B. Zhang and Q. Xu, Liquid-Phase Chemical Hydrogen Storage: Catalytic Hydrogen Generation under Ambient Conditions, *ChemSusChem*, 2010, **3**, 541–549.
6 U. Sikander, S. Sufian and M. A. Salam, A review of hydrotalcite based catalysts for hydrogen production systems, *Int. J. Hydrogen Energy*, 2017, **42**, 19851–19868.
7 Z. Liu, J. Li, S. Xue, S. Zhou, K. Qu, Y. Li and W. Cai, Pt/Mo2C heteronanosheets for superior hydrogen evolution reaction, *J. Energy Chem.*, 2020, **47**, 317–323.
8 C. Li and J. B. Baek, Recent Advances in Noble Metal (Pt, Ru, and Ir)-Based Electrocatalysts for Efficient Hydrogen Evolution Reaction, *ACS Omega*, 2020, **5**, 31–40.
9 X. Zhou, Y. Huang, W. Xing, C. Liu, J. Liao and T. Lu, High-quality hydrogen from the catalyzed decomposition of formic acid by Pd-Au/C and Pd-Ag/C, *Chem. Commun.*, 2008, 3540–3542.
10 J. A. Herron, J. Scaranto, P. Ferrin, S. Li and M. Mavrikakis, Trends in formic acid decomposition on model transition metal surfaces: A density functional theory study, *ACS Catal.*, 2014, **4**, 4434–4445.
11 Y. Cheng, X. Wu and H. Xu, Catalytic decomposition of hydrous hydrazine for hydrogen production, *Sustainable Energy Fuels*, 2019, **3**, 343–365.
12 Z. Wang, H. Zhang, L. Chen, S. Miao, S. Wu, X. Hao, W. Zhang and M. Jia, Interfacial Synergy of PtPd Nanoparticles Dispersed on Amine-Modified ZrSBA-15 in Catalytic Dehydrogenation of Ammonia Borane and Reduction of p-Nitrophenol, *J. Phys. Chem. C*, 2018, **122**, 12975–12983.
13 N. Gupta, O. Khavryuchenko, A. Villa and D. Su, Metal-Free Oxidation of Glycerol over Nitrogen-Containing Carbon Nanotubes, *ChemSusChem*, 2017, **10**, 3030–3034.
14 P. Veerakumar, P. Thanasekaran, T. Subburaj and K.-C. Lin, A Metal-Free Carbon-Based Catalyst: An Overview and Directions for Future Research, *C*, 2018, **4**, 54.
15 M. M. Titirici and M. Antonietti, Chemistry and materials options of sustainable carbon materials made by hydrothermal carbonization, *Chem. Soc. Rev.*, 2010, **39**, 103–116.
16 G. Mestl, N. I. Maksimova, N. Keller, V. V. Roddatis and R. Schlögl, Carbon Nanofilaments in Heterogeneous Catalysis: An Industrial Application for New Carbon Materials?, *Angew. Chem., Int. Ed.*, 2001, **40**, 2066–2068.
17 J. Zhang, X. Liu, R. Blume, A. Zhang, R. Schlögl and D. S. Su, Surface-Modified Carbon Nanotubes Catalyze Oxidative Dehydrogenation of *n*-Butane, *Science*, 2008, **322**, 73–77.
18 J. Zhang, D. S. Su, R. Blume, R. Schlögl, R. Wang, X. Yang and A. Gajović, Surface Chemistry and Catalytic Reactivity of a Nanodiamond in the Steam-Free Dehydrogenation of Ethylbenzene, *Angew. Chem., Int. Ed.*, 2010, **49**, 8640–8644.
19 M. Z. Rahman, M. G. Kibria and C. B. Mullins, Metal-free photocatalysts for hydrogen evolution, *Chem. Soc. Rev.*, 2020, **49**, 1887–1931.
20 K. Gong, F. Du, Z. Xia, M. Durstock and L. Dai, Nitrogen-Doped Carbon Nanotube Arrays with High Electrocatalytic Activity for Oxygen Reduction, *Science*, 2009, **323**, 760–764.
21 D. S. Su, G. Wen, S. Wu, F. Peng and R. Schlögl, Carbocatalysis in Liquid-Phase Reactions, *Angew. Chem., Int. Ed.*, 2017, **56**, 936–964.
22 A. Primo, F. Neatu, M. Florea, V. Parvulescu and H. Garcia, Graphenes in the absence of metals as carbocatalysts for selective acetylene hydrogenation and alkene hydrogenation, *Nat. Commun.*, 2014, **5**, 5291.
23 Y. Gao, D. Ma, C. Wang, J. Guan and X. Bao, Reduced graphene oxide as a catalyst for hydrogenation of nitrobenzene at room temperature, *Chem. Commun.*, 2011, **47**, 2432–2434.
24 H. P. Jia, D. R. Dreyer and C. W. Bielawski, Graphite oxide as an auto-tandem oxidation-hydration-aldol coupling catalyst, *Adv. Synth. Catal.*, 2011, **353**, 528–532.
25 C. Su, M. Acik, K. Takai, J. Lu, S. J. Hao, Y. Zheng, P. Wu, Q. Bao, T. Enoki, Y. J. Chabal and K. P. Loh, Probing the catalytic activity of porous graphene oxide and the origin of this behaviour, *Nat. Commun.*, 2012, **3**, 1–9.
26 D. R. Dreyer, H. P. Jia and C. W. Bielawski, Graphene oxide: A convenient carbocatalyst for facilitating oxidation and hydration reactions, *Angew. Chem., Int. Ed.*, 2010, **49**, 6813–6816.
27 M. A. Patel, F. Luo, M. R. Khoshi, E. Rabie, Q. Zhang, C. R. Flach, R. Mendelsohn, E. Garfunkel, M. Szostak and H. He, P-Doped Porous Carbon as Metal Free Catalysts for Selective Aerobic Oxidation with an Unexpected Mechanism, *ACS Nano*, 2016, **10**, 2305–2315.
28 A. Arami-Niya, M. S. Shafeeyan, W. M. A. W. Daud and A. Houshmand, Ammonia modification of activated carbon to enhance carbon dioxide adsorption: Effect of pre-oxidation, *Appl. Surf. Sci.*, 2011, **257**, 3936–3942.
29 M. S. Shafeeyan, W. M. A. W. Daud, A. Houshmand and A. Shamiri, A review on surface modification of activated carbon for carbon dioxide adsorption, *J. Anal. Appl. Pyrolysis*, 2010, **89**, 143–151.
30 W. M. A. W. Daud and A. H. Houshamnd, Textural characteristics, surface chemistry and oxidation of activated carbon, *J. Nat. Gas Chem.*, 2010, **19**, 267–279.
31 H. Yu, F. Peng, J. Tan, X. Hu, H. Wang, J. Yang and W. Zheng, Selective catalysis of the aerobic oxidation of cyclohexane in the liquid phase by carbon nanotubes, *Angew. Chem., Int. Ed.*, 2011, **50**, 3978–3982.
32 H. P. Jia, D. R. Dreyer and C. W. Bielawski, C–H oxidation using graphite oxide, *Tetrahedron*, 2011, **67**, 4431–4434.
33 J. Long, X. Xie, J. Xu, Q. Gu, L. Chen and X. Wang, Nitrogen-doped graphene nanosheets as metal-free catalysts for aerobic selective oxidation of benzylic alcohols, *ACS Catal.*, 2012, **2**, 622–631.
34 Y. Jiang, L. Yang, T. Sun, J. Zhao, Z. Lyu, O. Zhuo, X. Wang, Q. Wu, J. Ma and Z. Hu, Significant Contribution of

Intrinsic Carbon Defects to Oxygen Reduction Activity, *ACS Catal.*, 2015, **5**, 6707–6712.

35 C. Tang, H. F. Wang, X. Chen, B. Q. Li, T. Z. Hou, B. Zhang, Q. Zhang, M. M. Titirici and F. Wei, Oxygen Electrocatalysis: Topological Defects in Metal-Free Nanocarbon for Oxygen Electrocatalysis (Adv. Mater. 32/2016), *Adv. Mater.*, 2016, **28**, 7030.

36 L. Tao, Q. Wang, S. Dou, Z. Ma, J. Huo, S. Wang and L. Dai, Edge-rich and dopant-free graphene as a highly efficient metal-free electrocatalyst for the oxygen reduction reaction, *Chem. Commun.*, 2016, **52**, 2764–2767.

37 Q. Xiang, W. Yin, Y. Liu, D. Yu, X. Wang, S. Li and C. Chen, A study of defect-rich carbon spheres as a metal-free electrocatalyst for an efficient oxygen reduction reaction, *J. Mater. Chem. A*, 2017, **5**, 24314–24320.

38 Y. Qiu, S. Ali, G. Lan, H. Tong, J. Fan, H. Liu, B. Li, W. Han, H. Tang, H. Liu and Y. Li, Defect-rich activated carbons as active and stable metal-free catalyst for acetylene hydrochlorination, *Carbon*, 2019, **146**, 406–412.

39 Y. Gao, G. Hu, J. Zhong, Z. Shi, Y. Zhu, D. S. Su, J. Wang, X. Bao and D. Ma, Nitrogen-doped sp2-hybridized carbon as a superior catalyst for selective oxidation, *Angew. Chem., Int. Ed.*, 2013, **52**, 2109–2113.

40 Y. Jia, L. Zhang, A. Du, G. Gao, J. Chen, X. Yan, C. L. Brown and X. Yao, Defect Graphene as a Trifunctional Catalyst for Electrochemical Reactions, *Adv. Mater.*, 2016, **28**, 9532–9538.

41 I. Barlocco, S. Capelli, X. Lu, S. Tumiati, N. Dimitratos, A. Roldan and A. Villa, Role of defects in carbon materials during metal-free formic acid dehydrogenation, *Nanoscale*, 2020, **12**, 22768–22777.

42 I. Barlocco, S. Bellomi, S. Tumiati, P. Fumagalli, N. Dimitratos, A. Roldan and A. Villa, Selective decomposition of hydrazine over metal free carbonaceous materials, *Phys. Chem. Chem. Phys.*, 2022, **24**, 3017–3029.

43 S. Bellomi, I. Barlocco, S. Tumiati, P. Fumagalli, N. Dimitratos, A. Roldan and A. Villa, Effects of oxygen functionalities on hydrous hydrazine decomposition over carbonaceous materials, *Dalton Trans.*, 2023, **52**, 15871–15877.

44 Q. Yao, Y. Ding and Z.-H. Lu, Noble-metal-free nanocatalysts for hydrogen generation from boron-and nitrogen-based hydrides, *Inorg. Chem. Front.*, 2020, **7**, 3837–3874.

45 U. B. Demirci, Mechanistic insights into the thermal decomposition of ammonia borane, a material studied for chemical hydrogen storage, *Inorg. Chem. Front.*, 2021, **8**, 1900–1930.

46 S. Guan, Y. Liu, H. Zhang, R. Shen, H. Wen, N. Kang, J. Zhou, B. Liu, Y. Fan, J. Jiang and B. Li, Recent Advances and Perspectives on Supported Catalysts for Heterogeneous Hydrogen Production from Ammonia Borane, *Adv. Sci.*, 2023, **10**, 2300726.

47 I. Barlocco, S. Bellomi, B. M. C. Anghinelli, X. Chen, J. J. Delgado, M. Stucchi, L. Prati, K. Föttinger and A. Villa, Influence of nitrogen functional groups in carbon-based supports anchoring Pt nanoclusters and single atoms for efficient ammonia borane hydrolysis, *Chem. Commun.*, 2026, **62**, 4787–4790.

48 Y. Sun, Y. Du, W. Xue, L. Yu, H. Sun and Y. Tian, Enhanced catalytic hydrogenation of N-nitrosodimethylamine enabled by in situ hydrogen generation from ammonia borane hydrolysis on a bifunctional Rh/Al_2O_3-SBA-15 catalyst, *Appl. Catal., A*, 2026, **718**, 120883.

49 Y. Li, H. Huang, Q. Wei, S. Qiu, Y. Xia, F. Xu, L. Sun and H. Chu, Ruthenium Nanoparticles Anchored on Cobalt Oxide Married with Nitrogen and Phosphorus Co-Doped Carbon for Hydrolytic Dehydrogenation of Ammonia Borane, *ACS Catal.*, 2025, **15**, 9158–9170.

50 M. Minnucci, I. Barlocco, L. Prati, M. Stucchi, A. Villa, G. Di Carlo and F. Tessore, Rhodium porphyrin complexes as catalysts for ammonia borane hydrolytic dehydrogenation, *Dalton Trans.*, 2026, **55**, 2123–2134.

51 D. Xu, H. Jing, Y. Deng, X. Tian, W. Liu and F. Meng, Ultrafine Pd@NC catalyst for efficient tandem ammonia borane dehydrogenation and nitroarene hydrogenation, *Int. J. Hydrogen Energy*, 2025, **173**, 151261.

52 C. D. Mboyi, D. Poinsot, J. Roger, K. Fajerwerg, M. L. Kahn and J.-C. Hierso, The Hydrogen-Storage Challenge: Nanoparticles for Metal-Catalyzed Ammonia Borane Dehydrogenation, *Small*, 2021, **17**, 2102759.

53 S. Guan, Z. Yuan, S. Zhao, Z. Zhuang, H. Zhang, R. Shen, Y. Fan, B. Li, D. Wang and B. Liu, Efficient Hydrogen Generation from Ammonia Borane Hydrolysis on a Tandem Ruthenium–Platinum–Titanium Catalyst, *Angew. Chem.*, 2024, **136**(33), e202408193, DOI: 10.1002/ange.202408193.

54 I. Gerber, M. Oubenali, R. Bacsa, J. Durand, A. Gonçalves, M. F. R. Pereira, F. Jolibois, L. Perrin, R. Poteau and P. Serp, Theoretical and Experimental Studies on the Carbon-Nanotube Surface Oxidation by Nitric Acid: Interplay between Functionalization and Vacancy Enlargement, *Chem. – Eur. J.*, 2011, **17**, 11467–11477.

55 M. Roselló-Merino, R. J. Rama, J. Díez and S. Conejero, Catalytic dehydrocoupling of amine-boranes and amines into diaminoboranes: isolation of a Pt(II), Shimoi-type, η1-BH complex, *Chem. Commun.*, 2016, **52**, 8389–8392.

56 L. Luconi, E. S. Osipova, G. Giambastiani, M. Peruzzini, A. Rossin, N. V. Belkova, O. A. Filippov, E. M. Titova, A. A. Pavlov and E. S. Shubina, Amine boranes dehydrogenation mediated by an unsymmetrical iridium pincer hydride:(PCN) *vs.* (PCP) improved catalytic performance, *Organometallics*, 2018, **37**, 3142–3153.

57 A. Telleria, P. W. N. M. van Leeuwen and Z. Freixa, Azobenzene-based ruthenium(II) catalysts for light-controlled hydrogen generation, *Dalton Trans.*, 2017, **46**, 3569–3578.

58 G. Kresse and J. Hafner, Ab initio molecular dynamics for liquid metals, *Phys. Rev. B: Condens. Matter Mater. Phys.*, 1993, **47**, 558–561.

59 G. Kresse and J. Furthmüller, Efficiency of ab-initio total energy calculations for metals and semiconductors using a plane-wave basis set, *Comput. Mater. Sci.*, 1996, **6**, 15–50.

60 G. Kresse and J. Hafner, Ab initio molecular-dynamics simulation of the liquid-metalamorphous- semiconductor transition in germanium, *Phys. Rev. B: Condens. Matter Mater. Phys.*, 1994, **49**, 14251–14269.

61 J. P. Perdew, K. Burke and M. Ernzerhof, Generalized Gradient Approximation Made Simple, *Phys. Rev. Lett.*, 1996, **77**, 3865–3868.
62 C. Adamo and V. Barone, Toward reliable density functional methods without adjustable parameters: The PBE0 model, *J. Chem. Phys.*, 1999, **110**, 6158–6170.
63 J. P. Perdew, M. Ernzerhof and K. Burke, Rationale for mixing exact exchange with density functional approximations, *J. Chem. Phys.*, 1996, **105**, 9982–9985.
64 I. Barlocco, L. A. Cipriano, G. Di Liberto and G. Pacchioni, Modeling Hydrogen and Oxygen Evolution Reactions on Single Atom Catalysts with Density Functional Theory: Role of the Functional, *Adv. Theory Simul.*, 2022, **6**(10), 2200513, DOI: 10.1002/adts.202200513.
65 P. E. Blöchl, Projector augmented-wave method, *Phys. Rev. B: Condens. Matter Mater. Phys.*, 1994, **50**, 17953–17979.
66 D. Joubert, From ultrasoft pseudopotentials to the projector augmented-wave method, *Phys. Rev. B: Condens. Matter Mater. Phys.*, 1999, **59**, 1758–1775.
67 G. Di Liberto, L. A. Cipriano and G. Pacchioni, Universal Principles for the Rational Design of Single Atom Electrocatalysts? Handle with Care, *ACS Catal.*, 2022, **12**, 5846–5856.
68 S. Grimme, J. Antony, S. Ehrlich and H. Krieg, A consistent and accurate ab initio parametrization of density functional dispersion correction (DFT-D) for the 94 elements H-Pu, *J. Chem. Phys.*, 2010, **132**, 154104, DOI: 10.1063/1.3382344.
69 I. Barlocco, G. Di Liberto and G. Pacchioni, New scaling relationships for the oxygen evolution reaction on single atom catalysts, *Catal. Today*, 2024, **427**, 114409.
70 G. Di Liberto, L. Giordano and G. Pacchioni, Predicting the Stability of Single-Atom Catalysts in Electrochemical Reactions, *ACS Catal.*, 2024, **14**, 45–55.
71 J. K. Nørskov, T. Bligaard, A. Logadottir, J. R. Kitchin, J. G. Chen, S. Pandelov and U. Stimming, Trends in the Exchange Current for Hydrogen Evolution, *J. Electrochem. Soc.*, 2005, **152**, J23.
72 J. K. Nørskov, T. Bligaard, J. Rossmeisl and C. H. Christensen, *Towards the computational design of solid catalysts*, 2009, preprint, DOI: 10.1038/nchem.121.
73 E. Di Simone, G. Vilé, G. Di Liberto and G. Pacchioni, Decoding the Role of Adsorbates Entropy in the Reactivity of Single-Atom Catalysts, *ACS Catal.*, 2025, **15**, 447–456.
74 L. Prati, A. Villa, C. E. Chan-Thaw, R. Arrigo, D. Wang and D. S. Su, Gold catalyzed liquid phase oxidation of alcohol: the issue of selectivity, *Faraday Discuss.*, 2011, **152**, 353.
75 F. Tuinstra and J. L. Koenig, Raman Spectrum of Graphite, *J. Chem. Phys.*, 1970, **53**, 1126–1130.
76 P.-H. Tan, *Raman Spectroscopy of two-dimensional materials*, Springer, 2018, vol. 276.
77 K. N. Kudin, B. Ozbas, H. C. Schniepp, R. K. Prud'homme, I. A. Aksay and R. Car, Raman Spectra of Graphite Oxide and Functionalized Graphene Sheets, *Nano Lett.*, 2008, **8**, 36–41.
78 A. Eckmann, A. Felten, A. Mishchenko, L. Britnell, R. Krupke, K. S. Novoselov and C. Casiraghi, Probing the nature of defects in graphene by Raman spectroscopy, *Nano Lett.*, 2012, **12**, 3925–3930.
79 K. Maaz, *Raman spectroscopy and applications*, BoD–Books on Demand, 2017.
80 H. Murphy, P. Papakonstantinou and T. I. T. Okpalugo, Raman study of multiwalled carbon nanotubes functionalized with oxygen groups, *J. Vac. Sci. Technol., B: Microelectron. Nanometer Struct. Process., Meas. Phenom.*, 2006, **24**, 715–720.
81 R. Arrigo, M. Hävecker, S. Wrabetz, R. Blume, M. Lerch, J. McGregor, E. P. J. Parrott, J. A. Zeitler, L. F. Gladden, A. Knop-Gericke, R. Schlögl and D. S. Su, Tuning the acid/base properties of nanocarbons by functionalization via amination, *J. Am. Chem. Soc.*, 2010, **132**, 9616–9630.
82 D. C. Koningsberger, T. G. Ros, A. J. van Dillen and J. W. Geus, Surface oxidation of carbon nanofibres, *Chem. – Eur. J.*, 2002, **8**, 1151–1162.
83 L. R. Radovic, C. V. Mora-Vilches, A. J. A. Salgado-Casanova and A. Buljan, Graphene functionalization: Mechanism of carboxyl group formation, *Carbon*, 2018, **130**, 340–349.
84 A. Rasheed, J. Y. Howe, M. D. Dadmun and P. F. Britt, The efficiency of the oxidation of carbon nanofibers with various oxidizing agents, *Carbon*, 2007, **45**, 1072–1080.
85 H. Gong, S.-T. Kim, J. D. Lee and S. Yim, Simple quantification of surface carboxylic acids on chemically oxidized multiwalled carbon nanotubes, *Appl. Surf. Sci.*, 2013, **266**, 219–224.
86 R. Arrigo, M. Hävecker, S. Wrabetz, R. Blume, M. Lerch, J. McGregor, E. P. J. Parrott, J. A. Zeitler, L. F. Gladden, A. Knop-Gericke, R. Schlögl and D. S. Su, Tuning the Acid/Base Properties of Nanocarbons by Functionalization via Amination, *J. Am. Chem. Soc.*, 2010, **132**, 9616–9630.
87 S. Sengodan, R. Lan, J. Humphreys, D. Du, W. Xu, H. Wang and S. Tao, Advances in reforming and partial oxidation of hydrocarbons for hydrogen production and fuel cell applications, *Renewable Sustainable Energy Rev.*, 2018, **82**, 761–780.
88 G. Moussa, R. Moury, U. B. Demirci and P. Miele, Borates in hydrolysis of ammonia borane, *Int. J. Hydrogen Energy*, 2013, **38**, 7888–7895.
89 C.-H. Liu, Y.-C. Wu, C.-C. Chou, B.-H. Chen, C.-L. Hsueh, J.-R. Ku and F. Tsau, Hydrogen generated from hydrolysis of ammonia borane using cobalt and ruthenium based catalysts, *Int. J. Hydrogen Energy*, 2012, **37**, 2950–2959.
90 Q. Liu, W. Ran, W. Bao and Y. Li, A Review on Catalytic Hydrolysis of Ammonia Borane for Hydrogen Production, *Energies*, 2025, **18**, 1105.
91 S. Guan, Y. Liu, H. Zhang, R. Shen, H. Wen, N. Kang, J. Zhou, B. Liu, Y. Fan, J. Jiang and B. Li, Recent Advances and Perspectives on Supported Catalysts for Heterogeneous Hydrogen Production from Ammonia Borane, *Adv. Sci.*, 2023, **10**(21), 2300726, DOI: 10.1002/advs.202300726.
92 M. Yang, U. Raucci and M. Parrinello, Reactant-induced dynamics of lithium imide surfaces during the ammonia decomposition process, *Nat. Catal.*, 2023, **6**, 829–836.
93 C.-C. Hou, Q. Li, C.-J. Wang, C.-Y. Peng, Q.-Q. Chen, H.-F. Ye, W.-F. Fu, C.-M. Che, N. López and Y. Chen, Ternary Ni–Co–P nanoparticles as noble-metal-free catalysts to boost the hydrolytic dehydrogenation of ammonia-borane, *Energy Environ. Sci.*, 2017, **10**, 1770–1776.